# Origins of the pH Responsive Photoluminescence of Peptide Functionalised Au Nanoclusters

Laura Zanetti-Polzi,[1,⊥] Patrick Charchar,[2,⊥] Irene Yarovsky,[2,*] and Stefano Corni[1,3*]

*Corresponding authors: irene.yarovsky@rmit.edu.au (I.Y.); stefano.corni@unipd.it (S.C.)

[1]Istituto di Nanoscienze, Consiglio Nazionale delle Ricerche CNR-NANO, 41125 Modena, Italy
[2]School of Engineering, RMIT University, Victoria 3001, Australia
[3]Dipartimento di Scienze Chimiche, Università di Padova, 35131 Padova, Italy

**ABSTRACT:** Ultrasmall peptide-protected gold nanoclusters are a promising class of bio-responsive material exhibiting pH-sensitive photoluminescence. We present a theoretical insight into the effect peptide-ligand environment has on pH-responsive fluorescence, with the aim of enhancing the rational design of gold nanoclusters for bio-applications. Employing a hybrid quantum/classical computational methodology, we systematically calculate deprotonation free energies of N-terminal cysteine amine groups in proximity to the inherently fluorescent core of $Au_{25}$(Peptide)$_{18}$ nanoclusters. We find that subtle changes in hexapeptide sequence alter the electrostatic environment and significantly shift the conventional N-terminal amine p$K_a$ expected for amino acids free-in-solution by up to 5 p$K_a$ units. Our findings provide an insight into how the (de)protonation equilibrium of N-terminal amine and sidechain carboxyl groups cooperatively respond to solution pH changes; explaining the experimentally observed, yet elusive, pH-responsive fluorescence of peptide-functionalised $Au_{25}$ clusters.

**KEYWORDS:** Gold Nanoparticles, Peptide Ligands, Fluorescence, p$K_a$ Calculation, Quantum Mechanics/Molecular Mechanics

Atomically precise, photoluminescent gold nanoclusters (AuNCs) are an emerging class of materials with distinct and tuneable physicochemical properties. Due to their small size (2–3 nm diameter Au core), ligand-protected AuNCs exhibit strong quantum confinement effects that result in discrete molecule-like electronic structure and favourable optical qualities (*e.g.*, enhanced photostability and appreciable photoluminescence).[1-5] As such, the photophysical properties of AuNCs are attracting intense interest for applications that range from antimicrobial devices,[6] to biomedical theranostics,[7-9] and industrial photocatalysts.[10]

Over the past decade, a synergy of theoretical, experimental and computational advances has dramatically improved our understanding of AuNCs.[11-20] It is now well established that thiyl/thiolate-protected[21] $Au_m(SR)_n$ clusters contain a highly ordered, symmetrical nucleus, or "kernel", of Au(0) atoms that is capped by oligomeric "staple" motifs, $SR[Au(SR)]_x$ (*e.g.*, $x$ = 1: −RS−Au−SR−, $x$ = 2: −RS−Au−SR−Au−SR−, *etc.*).[22] For example, $Au_{25}(SR)_{18}$, one of the most extensively studied atomically precise AuNCs,[23] comprises an icosahedral $Au_{13}$ kernel surrounded by six dimeric staple motifs, $[Au_2(SR)_3]$.[24, 25] Due to these arrangements, surface ligands not only protect the AuNC metal core from aggregation and degradation,[26] they are dynamic[27] and integral structural components that influence the AuNCs' inherent and environmentally responsive physicochemical properties.[28, 29] It is therefore crucial to carefully and deliberately design capping-ligands that tailor AuNC functionality through: i) interior ligand–core interactions, which affect electronic structure, photoluminescence and optical absorption (*via* intra/interband transitions and charge transfer processes);[30-36] and ii) exterior ligand–environment interactions (*e.g.*, solvent, other nanoparticles, and intra/extracellular molecular components), which dictate AuNC solubility, selectivity, sensitivity, and responsiveness to environmental changes (*e.g.*, pH, salt, *etc.*).[37-39]

In the context of solubility, ligand chemistry determines whether a AuNC will be hydrophobic (organically-soluble) or hydrophilic (water-soluble). Hydrophobic $Au_m(SR)_n$ clusters (*e.g.*, R = aliphatic/aromatic hydrocarbons) have well-controlled atomic precision that is advantageous for catalysis,[40] crystallography,[41] and other structural characterisations.[42-44] On the other hand, hydrophilic clusters (*e.g.*, R = peptide/protein, or functional alkanethiols with –COOH, –OH, $–NH_2$ headgroups) are generally less deterministic in their size and structure but their non-toxicity, biocompatibility, and photostability improves their suitability for bio-applications.[45, 46] Peptide-ligands in particular possess an attractive set of features for functionalising biologically benign, bio-responsive, and water-soluble AuNCs since they can be systematically selected, designed, synthesised and controlled using standardised methods.[47, 48] For example, peptide-ligands on $Au_{25}$(Peptide)$_{18}$ biomedical probes can be optimised to sensitively and selectively respond to disease microenvironments *via* regulating AuNC *in vivo* catalytic activity,[49] or *in vitro* photoluminescence emission intensity.[50]

To explore and characterise the AuNC–biomolecular interface, theoretical and computational modelling approaches complement experimental findings and are an indispensable tool able to provide (sub)molecular scale information difficult to achieve experimentally.[51] The prototypical $Au_{25}(SR)_{18}$ cluster is fundamental to many computational studies since predicted properties can be directly

compared to available experimental data and its small size is ideal for first principles calculations (albeit mostly in vacuum or implicit solvent environments).[52-54] Quantum mechanical (QM) approaches, such as all-electron (*ab initio*) and density functional theory (DFT) methods, are vital for elucidating accurate structural, electronic, and optical properties of AuNCs, however, they can be computationally prohibitive for representing biologically relevant conditions.[55-58] To reduce computational cost, QM studies often: use truncated, simplified ligands that are water-insoluble (*e.g.*, R = H, $CH_3$, $CH_2CH_3$, benzene);[59] neglect or approximate solvent effects; and/or perform local geometry optimisations at absolute zero temperature (0 K), disregarding thermal fluctuations and conformational mobility of the ligands. In contrast, classical approaches based on molecular dynamics (MD) simulations can explore AuNC conformational ligand dynamics and thermodynamic properties in more realistic biological environments;[60-64] however, commonly used methodologies ignore electronic polarisation effects by requiring molecules to have static protonation states that are based on pre-assigned partial atomic charges. While the abovementioned techniques allow for many beneficial and accurate results to be obtained for specific systems and research questions, in isolation they may be less than ideal for studying the complex and dynamic phenomena that inherently pH-responsive functionalised AuNCs exhibit in an aqueous environment. Therefore, a multi-scale approach is desirable to synergistically combine classical MD conformational sampling for the biomolecular (peptide) components with accurate electronic structure calculations for the Au core and titratable residues.

Recently, some of us used a combined experimental and multi-scale computational strategy to explore a library of 23 hexapeptide-functionalised $Au_{25}$ nanoclusters, focussing on the role ligand–core interactions have in affecting the photoluminescent (PL) properties of the gold clusters.[65] The previously synthesised $[Au_{25}(SR)_{18}]$ nanoclusters were systematically and deliberately designed to assess how PL is affected by peptide structure alteration (e.g., N-terminal acetylation, primary sequence, removal/inclusion of titratable residues, and aromatic/hydrophobic character), as well as, varying environmental conditions (*e.g.*, pH and salt concentration). Amino acid sequence, nanoparticle hydration, and environmental pH were each shown to be capable of modulating $Au_{25}(Peptide)_{18}$ PL. Interestingly, several different peptide-ligand sequences imparted pH-responsive PL qualities to $Au_{25}$, with a significant PL intensity increase consistently observed when the solution pH was decreased from 7.5 to 5.5. The pH-sensitivity of the PL signal was not found to result from protonation state changes in the titratable histidine residues (whose p$K_a$ of ≈ 6 falls within the experimentally investigated pH interval), since pH-responsiveness of the systems was unchanged upon histidine replacement. Instead, it was hypothesised that the pH-sensitivity may originate from local environment induced changes in the protonation of the peptide N-terminal amine groups located in proximity to the inherently PL $Au_{13}$ kernel. The exact mechanism, however, that relates the N-terminal protonation/deprotonation equilibrium to the emission intensity remained elusive. Herein, we address this hypothesis by investigating three hexapeptide sequences for $Au_{25}(Peptide)_{18}$ systems whose experimental PL intensity is pH-responsive (Figure 1).[65] We compute local p$K_a$ values for the peptide N-terminal amines through applying a hybrid quantum/classical approach that employs both MD simulations and the perturbed matrix method (PMM). Termed the MD-PMM approach,[66] this technique has been previously used to compute molecular reduction potentials and reorganisation energies within proteins[67, 68] and in the presence of gold,[69] with recent extensions also allowing for the calculation of molecular p$K_a$ values.[70] This is achieved *via* the calculation of accurate deprotonation free energies while accounting for variations in the local chemical environment. In the current work we exploit these MD-PMM developments to determine deprotonation free energies for the N-terminal amine groups in the $Au_{25}(Peptide)_{18}$ systems and compare against the deprotonation free energy of methylammonium in solution to obtain local amine p$K_a$ values within the nanocluster environment. The calculated p$K_a$ values are then used to inform how the local environment near the kernel of the nanoclusters changes with pH to influence PL emission intensity.

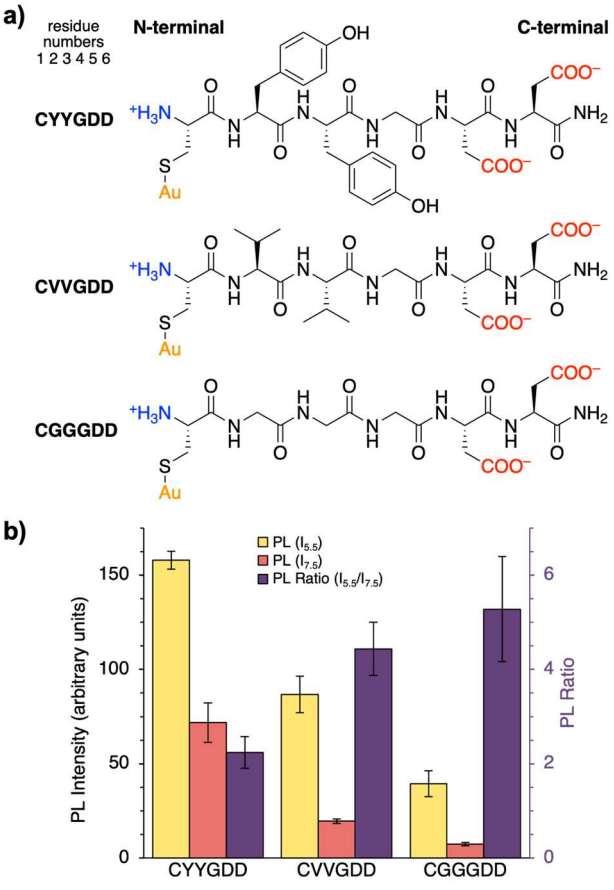


**Figure 1. a) The peptide-ligand sequences investigated, with varying amino acids at residue numbers 2 and 3. b) Effect of peptide-ligand sequence on the experimentally measured intensity of gold nanocluster photoluminescence (PL) at pH = 5.5 ($I_{5.5}$, yellow) and pH = 7.5 ($I_{7.5}$, red). The pH-sensitivity of the signals is presented as a PL ratio = $I_{5.5}/I_{7.5}$ (purple). Error bars represent standard deviation from triplicate measurements. Adapted with permission from Lin *et al.*[65] using the publicly available experimental raw data (DOI: 10.5281/zenodo.2202306). Copyright 2018, American Chemical Society.**

## RESULTS AND DISCUSSION

**Local N-terminal amine p$K_a$ calculations.** To explore the pH-sensitive PL of $Au_{25}$(Peptide)$_{18}$ and test the hypothesis that PL intensity is related to the (de)protonation equilibria of peptide N-termini in proximity to the Au core,[65] we compute local p$K_a$ values for N-terminal amine groups on three specific peptide-ligated AuNCs: $Au_{25}$(CYYGDD)$_{18}$, $Au_{25}$(CVVGDD)$_{18}$, and $Au_{25}$(CGGGDD)$_{18}$. Each hexapeptide-ligand (Figure 1a) consistently features a cysteine (C) residue at the N-terminus (necessary to anchor the peptides to the Au surface *via* covalent gold–sulphur bonding), two aspartic acids (DD) at positions 5 and 6 (essential for AuNC solubility), and a glycine (G) spacer at position 4. At positions 2 and 3 they vary in composition with either two tyrosine (YY), valine (VV) or glycine (GG) residues. The AuNCs investigated herein are strategically chosen from a broad set of previously investigated $Au_{25}$(Peptide)$_{18}$ nanoclusters[65] because they feature a particularly informative pH-responsiveness. They each exhibited a systematic increase in experimental PL when solution pH was decreased from 7.5 to 5.5, however, two residue variation in the peptide sequence following the Cys attachment (*i.e.*, in closest proximity to the Au core) distinctly impacted the resulting experimental PL intensities and pH-sensitivities.[65] It was found that the polarity, hydrophobicity, electron-withdrawing affinity, and size of the amino acids in positions 2 and 3 **(**Figure 1a) drastically influenced the measured PL intensities **(**Figure 1b).[65] Indeed, MD simulations further revealed that sidechain chemistry significantly affects the local chemical environment near the $Au_{13}$ kernel of $Au_{25}$(Peptide)$_{18}$ by means of imparting changes in: peptide layer thickness, conformation, and steric orientation; water penetration; electron density; and electrostatic potential.[65] Therefore, absolute PL intensities do not only depend on protonation/deprotonation equilibria but are intrinsically linked to more complex, environment-dependent, phenomena. For example, previous studies have established that aromatic rings (such as those in tyrosine) close to the gold kernel improve PL yields compared to aliphatic chains (such as those in valine).[30] For this reason, to investigate pH-sensitivity we focus on the ratio of the PL intensities at pH 5.5 and 7.5 rather than on absolute PL intensities, since the dimensionless ratio "normalises" the pH-sensitivity when making relative comparisons. As reported in Figure 1b, the tyrosine comprising sequence (CYYGDD) has the lowest PL intensity ratio (pH-sensitivity) of the clusters; valine replacement (CVVGDD) results in intermediate values; and the glycine rich (CGGGDD) ligated cluster features the highest PL ratio. In other words, the three $Au_{25}$(Peptide)$_{18}$ nanoclusters' PL can be ranked from least to most pH-sensitive as: CYYGDD < CVVGDD < CGGGDD.

Here we investigate how local electrostatic environment affects pH-sensitivity by exploiting the MD-PMM methodology (details provided in the Theory and Methods section, including the specific chemical groups treated at the quantum/classical level). Initially, we compute the deprotonation free energy of methylammonium in solution to be used as reference for all subsequent calculations (see Equation 4 in Theory and Methods). We recently showed that the solution p$K_a$ of methylammonium calculated with MD-PMM ($10.9 \pm 1.8$)[70] accurately reproduces the corresponding experimental value with excellent agreement (p$K_a^{ref}$ = 10.6).[71] In the present study, we recalculate the p$K_a$ of methylammonium using the AMBER99SB-ILDN force field[72] and obtain a slightly overestimated value by 1.8 p$K_a$ units. Although the change in force field leads to a modest discrepancy, it is within the standard error of the previous calculations and crucially ensures the reference deprotonation free energy is consistently estimated with the same interatomic potentials as the CVVGDD and $Au_{25}$(Peptide)$_{18}$ calculations. Furthermore, and most importantly, we are interested in computing relative p$K_a$ shifts of the selected peptides with respect to the methylammonium reference and, therefore, the absolute p$K_a$ overestimation does not relevantly affect the accuracy our calculations.

Next, we further test the reliability of the MD-PMM approach by computing the relative change in free energy needed to deprotonate the N-terminal amine group of a single CVVGDD peptide free-in-solution ($\Delta G$). Our results show that MD-PMM produces a N-terminal p$K_a$ for the solvated peptide that is essentially unaltered with respect to the reference p$K_a$ of methylammonium (Table 1). In the absence of a specific experimental estimate for the N-terminal p$K_a$ of solvated CVVGDD, we note that the calculated p$K_a$ is upshifted by ≈ 2.5–3 p$K_a$ units compared to typical amino-terminals in proteins (p$K_a$ ≈ 7.5). We also note that the presence of the negatively charged cysteine sidechain is consistent with an upshifted deprotonation free energy. In fact, the calculated p$K_a$ agrees very well with the experimental p$K_a$ of amine in zwitterionic cysteine (*i.e.*, 10.3)[73] in which deprotonation of the N-terminal is known to occur after thiol sidechain deprotonation.

Similarly, we predict the average N-terminal p$K_a$ value for each AuNC with different peptide-ligand sequence. Relative changes in free energy, $\Delta(\Delta G)$, presented in Table 1 describe how the dynamic perturbing electrostatic environments of each nanocluster (ligands, gold core, and solvent) affect the amount of energy needed to deprotonate one N-terminal amine group ($\Delta G_{AuNC}$) with respect to methylammonium in solution ($\Delta G_{ref}$). All three AuNCs are found to have a negative $\Delta(\Delta G)$, signifying the nanocluster environment encourages N-terminal amine deprotonation. For the AuNCs with bulkier residues in positions 2 and 3, $Au_{25}$(CYYGDD)$_{18}$ and $Au_{25}$(CVVGDD)$_{18}$, there is a significant change in deprotonation free energy (~20–30 kJ/mol), while for $Au_{25}$(CGGGDD)$_{18}$ the change is negligible.

It is important to differentiate between microscopic and macroscopic p$K_a$ values in systems that contain multiple titratable groups, since the protonation of one group can affect the proton dissociation propensity of another group (discussed further in the "Effect of protonation equilibria on pH-responsive PL" subsection below and in the Supporting Information).[74] Microscopic p$K_a$ values refer to the specific dissociation propensity of a single titratable group while the protonation states of all other groups are fixed. Macroscopic p$K_a$ values, such as those obtained from potentiometric titrations, describe the observable loss of a proton to change the total number of bound/dissociated protons across all titratable sites in the polyprotic system (*i.e.*, the net charge), regardless of the functional group involved. It should be emphasised that average microscopic p$K_a$ values are presented in Table 1. Values are calculated using $\Delta(\Delta G)$ averaged from the complete set of 18 local *micro*state transitions where the *first* N-terminal amine deprotonates in an environment

where the N-termini of 17 peptide-ligands are protonated and the aspartate carboxylate groups on all ligands are deprotonated (expressed as a ratio of positively charged protonated N-termini to negatively charged deprotonated aspartate residues, +17:–36). In other words, we consider all protonated N-terminal amine moieties in the "zwitterionic" reference state (+18:–36) to be equivalent in their affinity for protons. As such, regardless of the specific titratable sites involved, the 18 possible microstate transitions from the "zwitterionic" reference state (+18:–36) to the set of microstates with a singly deprotonated N-terminal (+17:–36) occur with equal probability and are characterised by the same average microscopic dissociation constant (p$K_a$, Table 1).

To gauge how deprotonated basic sites affect the microscopic p$K_a$ of successive N-terminal dissociations, we also perform a representative MD-PMM calculation of $Au_{25}(CVVGDD)_{18}$ going from a +1:–36 microstate to the "fully deprotonated" microstate, 0:–36. Here we find that N-terminal deprotonation to the "fully deprotonated" state (+1:–36 → 0:–36) is upshifted by +3.6 p$K_a$ units with reference to deprotonation from the "zwitterionic" state (+18:–36 → +17:–36). To a first-order approximation, the average between the upper and lower microscopic p$K_a$ estimates from the two extremes provides an approximate microscopic p$K_a$ for N-terminal amine in $Au_{25}(Peptide)_{18}$, implicitly taking into consideration amine–amine effects (Table 1, values in parentheses. The same half-shift of +1.8 p$K_a$ units is used for all three peptide-ligated AuNCs).

As shown in Table 1, $Au_{25}(CYYGDD)_{18}$ and $Au_{25}(CVVGDD)_{18}$ display considerable p$K_a$ downshifts with respect to methylammonium in solution (up to ≈ 6 $pK_a$ units). Although p$K_a$ differences of this magnitude are uncommon for titrating groups on the surface of proteins, experimental measurements of large p$K_a$ variations are not exceptional for amino acids in atypical environments (*e.g.*, buried in the protein interior and/or inside protein active sites).[75] Changes in p$K_a$ relative to solution values (up to ≈ 6–6.5 units) have been reported for several residues,[76-80] including a downshifted p$K_a$ of ≈ 4–5 units for the sidechain amino group of Lys.[81, 82] In the current work, significant p$K_a$ shifts are not unexpected since the N-terminal groups are embedded in an environment that differs substantially from that of surface groups in proteins: the amino groups are close to the Au surface, the tethering Au–S bond between the gold core and Cys residues restricts conformational rearrangement, and the N-terminal groups are situated in a crowded and relatively desolvated environment. Furthermore, if we consider the approximate microscopic p$K_a$ values accounting for amine–amine dependencies (Table 1, values in parentheses), the observed shifts are in line with many experimental protein measurements (≈ 3–4 $pK_a$ units).

**Table 1. Calculated deprotonation free energy differences, Δ(Δ*G*), and microscopic p$K_a$ values.**

| system | Δ(Δ*G*)[a] kJ/mol | N-terminal amine p$K_a$[b] | Δp$K_a$[b,c] |
|---|---|---|---|
| methylammonium | 0 | 10.6 | – |
| CVVGDD | +2 | 10.9 | +0.3 |
| $Au_{25}(CYYGDD)_{18}$ | –34 | 4.7 (6.5) | –5.9 (–4.1) |
| $Au_{25}(CVVGDD)_{18}$ | –26 | 6.1 (7.9) | –4.5 (–2.7) |
| $Au_{25}(CGGGDD)_{18}$ | –8 | 9.2 (11.0) | –1.4 (+0.4) |

[a]Δ(Δ*G*) = Δ*G* – Δ$G_{ref}$, with Δ$G_{ref}$ being the deprotonation free energy computed for methylammonium in solution. The standard error for Δ(Δ*G*) is ±7 kJ/mol. [b]Values in parentheses are upshifted by 1.8 units to implicitly consider amine–amine dependencies. [c]The p$K_a$ shifts relative to the experimental p$K_a$ of 10.6 for methylammonium.

Impact moieties have on electrostatic potential and deprotonation energy. To identify factors that determine the computed p$K_a$ trend of each system, we resolve the electrostatic potential ($\mathcal{V}$) exerted at the target N-terminal amine group's centre of mass into contributions from the system's constituent components (*i.e.*, the AuNC, the ligand peptides, the solvent and the counterions). Since the electrostatic potential heavily influences the perturbation operator in the MD-PMM methodology, $\mathcal{V}$ plays a major role in determining the N-terminal amine's electronic ground state energy change upon deprotonation, and hence the deprotonation free energy (see Theory and Methods).[83] An ensemble average of each component's contribution to $\mathcal{V}$ is obtained from the MD trajectories and in Figure 2 we report $\Delta(q\langle\mathcal{V}\rangle)$, the relative deprotonation energy contributions due to the mean electrostatic potential of $Au_{25}(CGGGDD)_{18}$ with respect to $Au_{25}(CYYGDD)_{18}$ and $Au_{25}(CVVGDD)_{18}$:

$$\Delta(q\langle\mathcal{V}\rangle)_{\mathrm{CGG-CYY}} = \Delta(q\langle\mathcal{V}\rangle)_{\mathrm{CGGGDD}} - \Delta(q\langle\mathcal{V}\rangle)_{\mathrm{CYYGDD}}$$

$$\Delta(q\langle\mathcal{V}\rangle)_{\mathrm{CGG-CVV}} = \Delta(q\langle\mathcal{V}\rangle)_{\mathrm{CGGGDD}} - \Delta(q\langle\mathcal{V}\rangle)_{\mathrm{CVVGDD}}$$

Given that $Au_{25}(CGGGDD)_{18}$ features the highest computed deprotonation free energy, which is also very similar to the deprotonation free energy of methylammonium in solution, examining $\Delta(q\langle\mathcal{V}\rangle)$ upon residue substitution allows us to elucidate the origin of the decreased p$K_a$ values for $Au_{25}(CYYGDD)_{18}$ and $Au_{25}(CVVGDD)_{18}$.

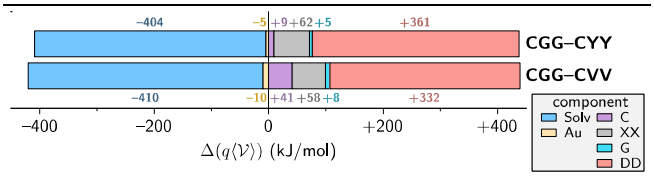


**Figure 2. Relative change in energy upon N-terminal amine deprotonation due to the mean electrostatic potential. $\Delta(q\langle\mathcal{V}\rangle)$ is presented for $Au_{25}(CYYGDD)_{18}$ and $Au_{25}(CVVGDD)_{18}$ relative to $Au_{25}(CGGGDD)_{18}$ and decoupled into terms for the: water molecules and counterions (Solv); the $Au_{25}$ core (Au); and individual peptide residues in their N-to-C-terminal order, *i.e.*, CXXGDD, where XX represents YY (top) and VV (bottom).**

Figure 2 reveals that solvent/counterions molecules as well as the peptide-ligands both strongly influence each system's mean electrostatic potential with opposing contributions. The solvent affects the electrostatic potential to exert a negative contribution to $\Delta(q\langle\mathcal{V}\rangle)$, whereas the peptides provide a positive contribution that is ~30 kJ/mol larger in magnitude. As such, the peptides' influence overcompensates the solvent effects, leads to a net positive $\Delta(q\langle\mathcal{V}\rangle)$ and,

subsequently, a decreased p$K_a$ for $Au_{25}(CYYGDD)_{18}$ and $Au_{25}(CVVGDD)_{18}$ when compared to $Au_{25}(CGGGDD)_{18}$. Interestingly, ~80% of the peptide-ligands' positive contributions result from the Asp residues. This indicates that the calculated p$K_a$ differences among the three ligand peptides is heavily modulated by the tendency of the $COO^-$ sidechain groups of the C-terminal Asp residues to interact with the $NH_3^+$ N-terminal amine groups.

The propensity for these end-to-end electrostatic interactions to occur is dictated by the chemistry of the peptide-ligand sequence that, in turn, impacts on the overall conformation of the system. We recently showed that the glycine-rich sequence in $Au_{25}(CGGGDD)_{18}$ causes the peptide-ligands to almost exclusively adopt collapsed conformations, with short distances measured between N-terminal Cys and C-terminal Asp residues.[65] On the contrary, in $Au_{25}(CYYGDD)_{18}$ and $Au_{25}(CVVGDD)_{18}$ more elongated conformations were sampled (Figure S1).[65] Here we establish that solvent significantly affects the electrostatic potential around the nanocluster core to encourage an increase in N-terminal amine p$K_a$ of $Au_{25}(CYYGDD)_{18}$ and $Au_{25}(CVVGDD)_{18}$ with respect to $Au_{25}(CGGGDD)_{18}$. This contribution can be explained by investigating how the average number of surface-bound water molecules differ between the three systems (Figure S2). In the $Au_{25}(CGGGDD)_{18}$ system, the condensed ligand layer reduces the amount of internalised water close to the gold surface with respect to $Au_{25}(CYYGDD)_{18}$ and $Au_{25}(CVVGDD)_{18}$.[65] This implies that the presence of water near the amino groups has a stabilising effect on the protonated form ($NH_3^+$) to determine a higher p$K_a$. Nonetheless, the stabilising effect is overcompensated by the contribution of surface-proximate Asp residues. Interestingly, Figure 2 reveals that there is a small, but non-negligible, positive contribution from the residues in positions 2 and 3 when they are mutated from two Gly to two Val/Tyr residues. We suggest that this contribution may also be connected to the abovementioned reduced number of surface-bound water molecules in $Au_{25}(CGGGDD)_{18}$. The absence of these water molecules is in fact accompanied by an increase in the number of electron-rich atoms near the gold surface (Figure S3),[65] and we suspect that these atoms, such as the polar backbone atoms of glycine residues 2 and 3 in $Au_{25}(CGGGDD)_{18}$ further stabilise $NH_3^+$ to give a higher p$K_a$.

Effect of protonation equilibria on pH-responsive PL. The importance of the Asp residues' influence on the amino group p$K_a$ variation suggests that Asp residues play a crucial role in influencing the pH-responsiveness of the investigated systems. Based on the above results, we believe these groups are implicated in tuning the PL signal intensity upon pH increase. In particular, the calculated p$K_a$ values for the three peptides and their relative differences suggest that the pH dependence is partially correlated to electrostatic interactions between positively charged N-terminal groups and negatively charged Asp sidechains. Electrostatic $NH_3^+\cdots COO^-$ interactions affect the dielectric environment around the AuNC core and therefore the balance between the population of deprotonated and protonated $NH_2/NH_3^+$ and $COO^-/COOH$ groups should be carefully considered to rationalise the pH-responsiveness of the AuNCs' PL signal. In fact, the Asp sidechain is itself a titratable group whose protonation/deprotonation equilibrium can affect the behaviour of the system. Although the typical solution p$K_a$ for an Asp sidechain is ≈4[73] and below the lowest investigated pH, it cannot be overlooked that each AuNC features a total of 36 Asp residues (*i.e.*, 18 peptide-ligands each with two Asp residues at the C-termini). The short length of the tethered hexapeptide-ligands and the steric arrangement in the $Au_{25}(Peptide)_{18}$ structures enable relatively dense packing of Asp residues resulting in high local concentrations of negative charge. This highly charged environment may arguably raise the Asp sidechain p$K_a$ to a value within the experimentally investigated pH interval. Therefore, by increasing solution pH from 5.5 to 7.5, the proportion of deprotonated $COO^-$ Asp sidechains is expected to increase, while the population of protonated $NH_3^+$ terminals will increase according to the computed p$K_a$ values (Figure 3a). To evaluate the microscopic p$K_a$ of Asp residues, we use MD-PMM to compute deprotonation free energies for the 36 Asp sidechains of each peptide-ligated AuNC. The results show that, on average, the microscopic p$K_a$ of Asp is upshifted by ~3 units with respect to the solution case. Therefore, the p$K_a$ of the Asp residues in our peptides is ~7 (further detailed in the Supporting Information and Table S1).

The calculated p$K_a$ values for Asp sidechains, as well as those for the N-terminal amine groups of $Au_{25}(CYYGDD)_{18}$ and $Au_{25}(CVVGDD)_{18}$, are found to coincide with the experimentally investigated pH interval of 5.5–7.5. This suggests that the pH-responsive PL of $Au_{25}(Peptide)_{18}$ can be rationalised by considering the combined protonation/deprotonation equilibria of N-terminal amine groups and aspartic acid sidechain carboxyl groups, and their electrostatic interactions, at different solution pHs. It is therefore necessary to relate the calculated proton affinities (*i.e.*, microscopic p$K_a$ values) to the overall polyprotic equilibria of the systems (*i.e.*, macroscopic p$K_a$ values). Below we employ two approaches, with roots in statistical mechanics, that have been beneficial in describing polyprotic titration within proteins,[74] namely, "the null model" and "the smeared-out charge (mean-field) model" (details provided in the Supporting Information).

The null model provides the simplest first-order approximation of the polyprotic equilibrium by considering all titrating sites to be sufficiently separated from each other so that their microscopic proton affinities (p$K_a$) are unchanged with respect to the protonation state of neighbouring sites. Although this approximation provides qualitatively reasonable results (Figure S4) that correlate to the experimental pH-responsive PL trends, the null model, by definition, does not support the N-terminal microscopic p$K_a$ upshift obtained from MD-PMM considering amine–amine dependencies (Table 1).

Instead, a smeared-out charge approach is utilised to appropriately estimate macroscopic p$K_a$ values with dependent titratable groups. Within this mean-field model, the protonation state of chemically equivalent sites influences the microscopic p$K_a$ of successive dissociations, *i.e.*, N-terminal amine–amine dependencies or Asp sidechain carboxyl–carboxyl dependencies. From a macroscopic description (see Supporting Information), this approach provides the results depicted in Figure 3a. More specifically, ~50% Asp residues will be deprotonated ($COO^-$) at solution pH = 5.5 whereas ~90% Asp residues will be deprotonated at pH = 7.5. As for the peptide-ligands' N-terminal amine groups: $Au_{25}(CYYGDD)_{18}$ is expected to have ~65% of N-terminals

protonated ($NH_3^+$) at pH = 5.5 and ~30% at pH = 7.5; $Au_{25}(CVVGDD)_{18}$ will have ~90% of N-terminals protonated at pH = 5.5 and ~55% at pH = 7.5; and $Au_{25}(CGGGDD)_{18}$ is predicted to have all ligand N-terminals protonated at both pHs.

Building on the suggestion of Lin *et al.* that deprotonated amine moieties (*i.e.*, electron donating groups) close to the gold kernel promote PL quenching, here we broaden the picture by considering any event that increases the ligand-to-metal (LTM) electron-donating capability of the peptide layer as an event that promotes PL quenching. On the contrary, any event that decreases LTM electron donation (*i.e.*, increases electron-withdrawing capability) should be considered as PL enhancing. For example, the protonation of a N-terminal amine nitrogen simultaneously removes a lone pair of electrons while also adding a positive (*i.e.*, electron-withdrawing) group close to the kernel, and this has the net effect of strongly enhancing PL. In contrast, the presence of $COO^-$ groups close to the gold kernel improves electron-donating capabilities and thus promotes PL quenching. In relation to pH-sensitivity, we reason that although proximal $COO^-$ groups are expected to induce quenching, due to steric and screening effects their main influence is in mitigating the $NH_3^+$ electron-withdrawing capacity. In other words, the establishment of a $NH_3^+/COO^-$ interaction decreases the electron-withdrawing ability of $NH_3^+$, and thus is detrimental to PL yield. For clarity, herein we refer to these $NH_3^+/COO^-$ interactions as "shielding" of $NH_3^+$ from the nanocluster kernel, and the corresponding $NH_3^+$ and $COO^-$ groups as being "shielded" $NH_3^+$ and $COO^-$ groups. To relate the experimental PL trend with the microscopic view revealed by our simulations, we identify which events take place as a function of pH, and to what extent they are expected to modify the electron-donating capabilities of the gold-proximal groups.

In Lin *et al.* we suggested in fact that the protonation equilibria of these two titratable groups ($NH_3^+/COO^-$) is likely linked to the pH-sensitivity of the PL signal,[65] we reveal here that there is indeed a correlated influence and rationalise the effect. Although all systems are expected to exhibit similar Asp sidechain deprotonation as the solution pH increases, the varied peptide sequences alter the local chemical environment to affect the amount of unshielded charge groups close to the nanocluster kernel (Figure 3b). Upon pH increase, for CYYGDD the net effect is a reduction in the number of shielded $NH_3^+$ that are transformed into deprotonated $NH_2$ groups (Figure 3b). This type of change has a minor influence on altering PL since both transforming groups have similar, and minimal, PL quenching capabilities. In addition, very few unshielded $COO^-$ groups will be electrostatically drawn close to the gold core at either pH 5.5 or at pH 7.5. Thus, unshielded $COO^-$ is also unlikely to affect the PL yield. This analysis justifies CYYGDD exhibiting the lowest experimental pH-sensitivity, as expressed by the PL ratio (Figure 1b). On the contrary, for CGGGDD, a pH shift from 5.5 to 7.5 concurrently increases the amount of shielded $NH_3^+$ and unshielded $COO^-$ groups near the NC surface (Figure 3b). These two effects are expected to contribute a significant amount of quenching upon pH increase, and indeed this is evidenced by CGGGDD undergoing a relative decrease of its PL intensity by ~81% at the higher pH. Finally, the changes underwent by the CVVGDD system are intermediate between those described for CYYGDD and for CGGGDD, coherently with its intermediate experimental pH sensitivity.

Furthermore, when $NH_3^+/COO^-$ interactions were experimentally removed by design *via* acetyl N-terminal capping, this was shown to suppress the pH-responsiveness of the PL signal while simultaneously enhancing the PL intensity compared to the corresponding uncapped AuNCs.[65] In MD simulations of these acetyl-capped systems, the absence of strong electrostatic interactions between the peptide termini lead to an overall AuNC volume increase with a thicker peptide layer shielding the nanoclusters from solvent interactions and correlating with an enhanced emission intensity.[65] This strongly supports the rationale proposed here that the onset of $NH_3^+/COO^-$ interactions modulate the PL signal. Nonetheless, we recognise that the computational analysis presented simplifies a rather complex scenario. In the investigated systems there is a large number of titratable groups and their intricate and interdependent protonation/deprotonation equilibria are treated here in a simplified manner (*e.g.*, all titratable sites are considered equivalent, ionic strength effects are neglected).[84] Although this may non-trivially affect the overall pH-responsiveness of the systems, taking all into consideration, we demonstrated the model we propose here agrees with, and rationalises, the experimental observations.

## CONCLUSIONS

Through the systematic calculation of local environment-dependent deprotonation free energies, we provide insight into how the PL emission intensity of peptide-coated $Au_{25}$ is inversely related to solution pH, in line with previous experimental and multi-scale computational observations.[65] Utilising the MD-PMM approach, we deliver a simplified computational description of the multifaceted, complex, and non-trivial coupling that a large number of ionisable groups impose on the interdependent protonation/deprotonation equilibria of $Au_{25}(Peptide)_{18}$ nanoclusters. We find that the pH-sensitive nature of $Au_{25}$'s PL emission can be explained *via* pH-tuneable electrostatic interactions occurring between titratable N-terminal amine and C-terminal aspartate moieties. Our calculations reveal that hexapeptide-ligand sequence mutations modulate the crowded environment near the Au–S bonding interface of $Au_{25}(Peptide)_{18}$ nanoclusters to significantly shift p$K_a$ values of individual N-terminal amine groups by up to 5 p$K_a$ units. Our results highlight the microscopic impact that $NH_3^+$ and $COO^-$ electrostatic interactions have on the polyprotic equilibria of $Au_{25}(Peptide)_{18}$ nanoclusters. As such, they provide guidance for the deliberate design and control of peptide sequence, solution pH, electrostatic environment near the PL $Au_{25}S_{18}$ centre of the nanoclusters, and ultimately, the PL emission intensity. The insight from this work provides a functional platform for the engineering of bio-responsive materials. Our findings aid the rational design of biologically nucleated gold nanoparticles to be used for several relevant applications. For instance, the bottom-up engineering of peptide coatings with biocompatibility and biologically specific functionalities can be pursued together with the deliberate modulation of their photoluminescent properties.

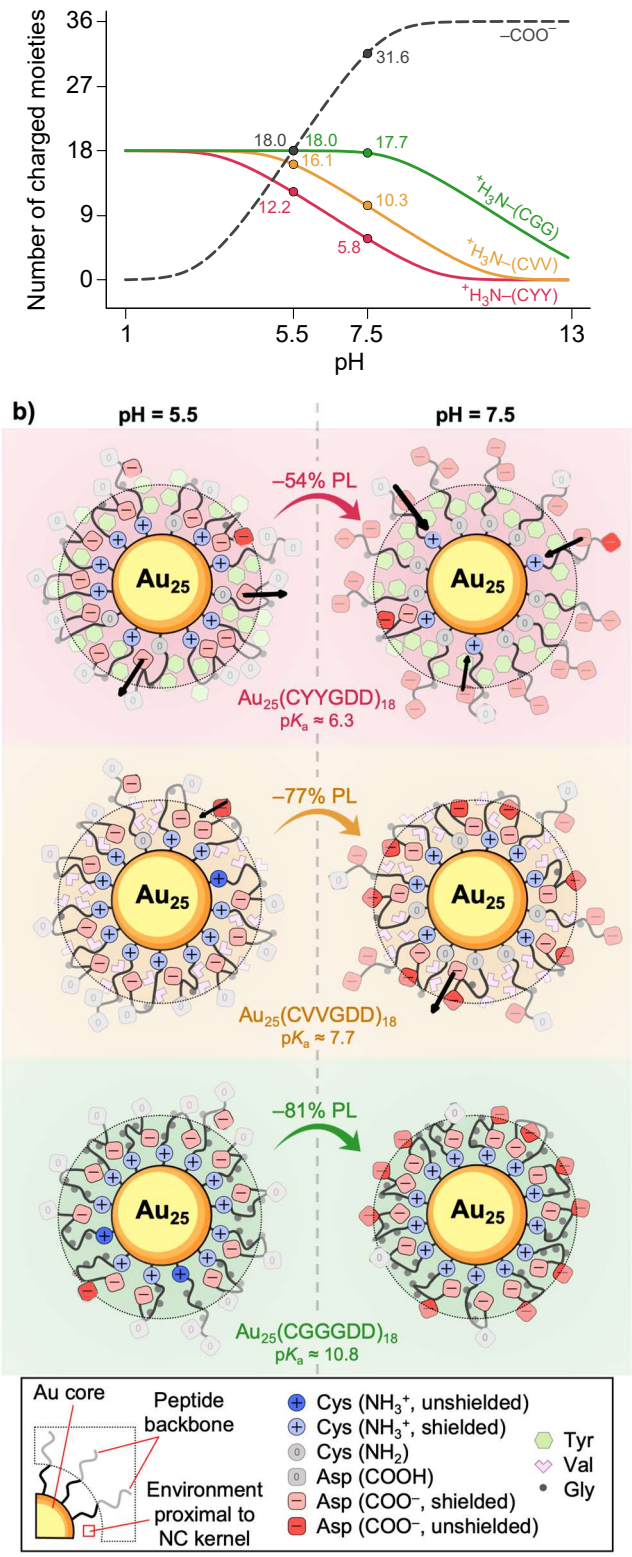


**Figure 3. a) Number of charged moieties as a function of pH, as obtained using the mean-field model for chemically equivalent groups that display interdependent proton affinities. b) Schematics showing the protonation equilibria for the investigated peptide-ligated $Au_{25}$ nanoclusters at pH 5.5 and 7.5. For clarity, the experimentally measured pH-sensitivity of each system[65] is presented as a percent decrease going from pH 5.5 to 7.5, which is derived from the PL Ratio $(I_{7.5}/I_{5.5}–1)\times100\%$. The influence of charged moieties on the photoluminescence (PL) of the $Au_{25}S_{18}$ kernel is expected to be *shielded*/mitigated when opposite charge groups ($NH_3^+$/$COO^-$) are interacting with each other.**

## THEORY AND METHODS

The molecular dynamics–perturbed matrix method. In the MD-PMM computational strategy,[66] a system is partitioned into two regions: i) the quantum centre (QC), which contains atoms associated to the processes of interest requiring a quantum level of treatment (*i.e.*, the titratable group in the present case); and ii) the remainder of the system (the environment), which affects the properties of the QC *via* an electrostatic perturbation obtained from the system's atomistic classical MD configurations. Unlike other QM/MM approaches where the QC is expensively (and often prohibitively) simulated with *ab initio* MD in the perturbing environment of the non-QM region, in the MD-PMM the perturbation operator is expanded so that the presence of the environment is applied *a posteriori* onto the instantaneous quantum properties of the QC. This approximation allows perturbed quantum properties to be estimated efficiently for a comprehensive ensemble of configurations obtained from extended classical MD simulations of the whole system (including the quantum part). The (unperturbed) quantum properties of the isolated QC are calculated quantum-chemically in vacuum, *i.e.*, in the gas phase. Then, for each (whole system) configuration/frame generated by all-atom classical MD simulations, the QC Hamiltonian operator is perturbed by the distinct electrostatic field resulting from the environment's instantaneous atomic arrangement. Therefore, the electronic Hamiltonian operator $\hat{H}$ of the QC embedded in the perturbing environment of configuration $i$ is expressed as:

$$\hat{H}_i = \hat{H}^0 + \hat{V}_i \qquad (1)$$

where $\hat{H}^0$ is the QC unperturbed electronic Hamiltonian obtained considering just the isolated QC and $\hat{V}_i$ is the perturbation operator from environment configuration *i*. In typical PMM calculations, the perturbing electric field provided by the environment's atomic charges is used to determine the perturbation operator $\hat{V}$ *via* a multipolar expansion centred on the QC's centre of mass, $\mathbf{r}_0$ (QC-based expansion). In the present work, we employ a recent development of the PMM approach that was refined to include higher order terms by expanding the perturbation operator around each individual atom of the QC (atom-based expansion).[66] When constructing the perturbed Hamiltonian matrix, the atom-based expansion is used for the diagonal elements, whereas the non-diagonal matrix elements of the perturbation operator are obtained by using the QC-based perturbation operator expansion within the dipolar approximation. Therefore, the elements $V_{I,J}$ of the perturbation operator matrix element between the electronic states $I$ and $J$ can be expressed as:

$$V_{I,J} \cong \delta_{IJ} \sum_N \mathcal{V}(\mathbf{R}_N) q_{N,I} - (\mathbf{E}(\mathbf{r}_0) \cdot \boldsymbol{\mu}_{I,J})(1 - \delta_{IJ}) \qquad (2)$$

with $N$ running over all QC atoms, $\mathbf{R}_N$ the nucleus position of the $N$th atom of the QC and $q_{N,I}$ the corresponding atomic charge in the state $I$, $\mathcal{V}$ the electrostatic potential exerted by the perturbing environment, $\mathbf{E}$ the perturbing electric field ($\mathbf{E} = -\partial V/\partial \mathbf{r}$), $\boldsymbol{\mu}_{I,J}$ the QC transition dipole moment, and $\delta_{IJ}$ the Dirac delta function.

At each frame of the MD simulation ensemble, the perturbed electronic Hamiltonian matrix is constructed and diagonalised to provide a continuous trajectory of perturbed eigenvalues and eigenvectors. The QC's instantaneous perturbed quantum observable of interest is then evaluated at each frame of the trajectory.

Calculation of p$K_a$ values. The MD-PMM approach is useful for efficiently estimating local acid dissociation constants ($K_a$), where p$K_a$ = –log($K_a$), through the calculation of deprotonation free energies (comprehensive description can be found in [70]). Compared to other p$K_a$ predicting methodologies, the MD-PMM approach

investigates quantum properties of the titratable group while exploiting extensive MD sampling of the environment (in the present case, $1.8\times10^6$ conformations are used for each peptide) to give insights into the molecular determinants affecting the free energy change. In addition, MD-PMM does not require the use of any ad-hoc parameters that need to be adjusted depending on the system or chemical process under investigation.[85-87] Therefore, it can be applied in non-standard environments, as is the present case. Briefly, gas-phase QM calculations are performed for the protonated (acid) and deprotonated (base) QC of interest, as well as MD simulations with the whole system explicitly solvated in water and the QC in a fixed protonation state (either acidic or basic). The QM calculations provide the acid and base QCs' unperturbed electronic Hamiltonians ($\hat{H}^0$), whereas the MD simulations determine the environment that gives an ensemble of perturbation operators ($\hat{V}$). Exploiting Equation 1, perturbed Hamiltonians for the acid and base QCs are established ($\hat{H}$) and used to calculate $\Delta\mathcal{U}_e$, the perturbed electronic ground state energy change of the QC upon deprotonation (*acid* → *base*). Subsequently, the Gibbs free energy change $\Delta G$ upon deprotonation is given by:

$$\Delta G \cong -k_B T \ln\langle e^{-\beta\Delta\mathcal{U}_e}\rangle_{acid} \cong -k_B T \ln\langle e^{-\beta\Delta\mathcal{U}_e}\rangle_{base} \qquad (3)$$

where $k_B$ is the Boltzmann constant, T is temperature, $\beta = 1/k_B T$, and the subscript on the angled brackets indicates that both energy change and ensemble-averaging are obtained in the perturbing environment of a static protonation ensemble, *i.e.*, the protonated (acid) or deprotonated (base) ensemble. In other words, the environment configurations that perturb the QC's QM properties are obtained from MD simulations that have the QC in a fixed protonation state. Note that although MD-PMM can be used to calculate absolute free energy differences by averaging $\Delta G$ obtained in both the protonated and deprotonated ensembles,[70] in the present case we are interested in relative p$K_a$ shifts (Equation 4) and therefore a single MD simulation in a fixed (protonated) ensemble provides a sufficient $\Delta G$ estimate. When computing absolute p$K_a$ values, the accuracy of the absolute estimate is determined by the accuracy determined by the accuracy of multiple factors, namely: the calculated $\Delta G$, the gas-phase quantum chemical calculations, and the experiment-based estimates used to obtain the p$K_a$ values (*i.e.*, the gas-phase standard reaction free energy and the solvation free energy of the proton).[70] This leads to a relatively high error propagation for absolute p$K_a$ values (≈ 1.7 p$K_a$ units). Conversely, $\Delta$p$K_a$ shifts depend only on the accuracy of the calculated $\Delta G$ (≈ 1 p$K_a$ unit), which is in line with estimates from other computational methods (*e.g.*, QM/MM or continuum electrostatics), as thoroughly discussed in [70].

For the specific task of computing the N-terminal amine p$K_a$ of $Au_{25}$ peptide-ligands, the deprotonation free energy of a single amine group in $Au_{25}$(Peptide)$_{18}$ ($\Delta G_{AuNC}$) is calculated. We investigate the N-terminal amine p$K_a$ of three representative hexapeptide-ligand sequences that vary only in residue positions two and three (CYYGDD, CVVGDD, and CGGGDD; Figure 1a). These amino acid substitutions were specifically chosen since they are known to affect the ligands' electron-withdrawing affinity, hydrophobicity, steric packing, intermolecular interactions and, ultimately, variations in $Au_{25}$(Peptide)$_{18}$ PL pH-responsiveness.[65] Gas-phase QM calculations are performed on methylammonium ($CH_3NH_3^+$) and methylamine ($CH_3NH_2$) molecules to obtain the unperturbed $\hat{H}^0$ for the acid and base $QC_{QM}$, respectively. Then, from every frame of our MD simulations, the N-terminal amino and alpha carbon methine moieties ($-C_\alpha HNH_3^+$) on one peptide-ligand are selected as the $QC_{MD}$ to extract the perturbing electrostatic environment of: the solvent, the $Au_{25}$ nanocluster, the other 17 peptide-ligands bound to the AuNC, as well as the non-$QC_{MD}$ remainder of the chosen peptide-ligand (Figure 4). This is systematically repeated, selecting the $QC_{MD}$ from a different $Au_{25}$(Peptide)$_{18}$ ligand each time, so that the overall distribution of $\Delta G_{AuNC}$ values encompasses all 18 N-terminal groups (at all MD frames). The p$K_a$ estimate for N-terminal amine is therefore:

$$pK_a = \Delta pK_a + pK_a^{ref} \cong \frac{\Delta G_{AuNC} - \Delta G_{ref}}{2.303\, k_B T} + pK_a^{ref} \qquad (4)$$

where $pK_a^{ref}$ of 10.6 is the experimental p$K_a$ of methylammonium,[71] and the reference deprotonation free energy of methylammonium free-in-solution ($\Delta G_{ref}$) is calculated with the entire solute molecule as the $QC_{QM}$ and all solvent atoms (from MD) contributing to the perturbing environment.[70] Following the above procedure, we also estimate the p$K_a$ value for a single peptide free-in-solution, where the same N-terminal group of the peptide is considered as the $QC_{MD}$ that is perturbed by the solvent and the rest of the peptide. To estimate how deprotonated basic sites affect the microscopic p$K_a$ of successive N-terminal dissociations (see Results and Discussion section), we calculate the p$K_a$ shift $Au_{25}$(CVVGDD)$_{18}$ undergoes when 1 N-terminal deprotonates in the presence of 17 protonated N-termini (+18:–36 → +17:–36) and compare to the p$K_a$ shift obtained when 1 N-terminal deprotonates in the presence of 17 deprotonated N-termini (+1:–36 → 0:–36). Considering the large difference in the statistical sampling between the two abovementioned microstates (for the first one we performed the calculation on 18 titratable sites, for the second one on a single site), we estimate the free energy difference between the two microstate transitions using the linear response approximation, *i.e.*, by assuming a Gaussian distribution for the energy change upon deprotonation and considering the mean values of the deprotonation energy obtained along the MD trajectories. With respect to the full calculation of $\Delta(\Delta G)$, the linear response approximation is less affected by inaccuracies due to sampling issues. All investigated deprotonation processes are listed in Table 2.

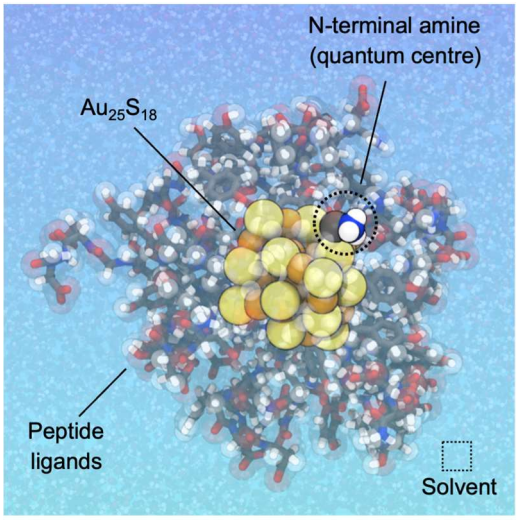


**Figure 4. Representative snapshot from molecular dynamics (MD) simulation highlighting the Quantum Centre ($QC_{MD}$) and perturbing environments for the $Au_{25}$(CYYGDD)$_{18}$ nanocluster.**

Quantum mechanical calculations. To calculate p$K_a$ values for N-terminal amine in $Au_{25}$(Peptide)$_{18}$, QM calculations for methylammonium (protonated QC) and methylamine (deprotonated QC) were previously performed[70] and are here only briefly summarised. For both QC protonation states, the isolated molecule ($CH_3NH_3^+$ or $CH_3NH_2$) is geomet ry optimised in the gas-phase and used to obtain the unperturbed electronic eigenfunctions and properties. Calculations are performed in the Gaussian09 package,[88] using the Density Functional Theory (DFT) approach[89] with the 6-31+G(d) basis set[90] and the B3LYP functional.[91] Time-dependent DFT (TD-DFT) is used with the same functional and basis set for evaluating the properties of the excited states. A 6×6-dimensional Hamiltonian matrix is evaluated and diagonalised at each MD simulation step using the electrostatic environment produced by non-QC atoms (see MD-PMM methodology above). Charges employed in the atom-based expansion procedure are obtained by fitting the classical electrostatic potential outside the molecule to the corresponding QM potential *via* the electrostatic potential fit procedure (ESP charges).[92]

Molecular dynamics simulations. Explicit solvent MD simulations were used to sample the conformational landscapes of each system (Table 2) and generate equilibrated ensembles of atomic configurations. Specifically, we modelled: methylammonium, the CVVGDD peptide, and the $Au_{25}$(CYYGDD)$_{18}$, $Au_{25}$(CVVGDD)$_{18}$, and $Au_{25}$(CGGGDD)$_{18}$ nanoclusters. MD for all systems was performed using the GROMACS 4.6.5 software[93] and the all-atom AMBER99SB-ILDN force field,[72] with equivalent simulation conditions and settings as described in [65] (further details given in the Supporting Information).

In peptide-containing systems, N-termini were protonated ($NH_3^+$) and C-termini were capped with a $NH_2$ moiety, consistent with the experimental ligands.[65] For $Au_{25}$(CVVGDD)$_{18}$, an additional simulation was performed with 17 deprotonated ($NH_2$) N-termini and 1 protonated N-terminal, which was then used as quantum centre for the deprotonation free energy calculation. For CVVGDD (in solution), MD was conducted with the N-terminal cysteine's thiol sidechain deprotonated to best represent the N-terminal amine deprotonation process (Table 2), since the p$K_a$ of thiol in zwitterionic cysteine is approximately 2 p$K_a$ units lower than the N-terminal amino group (*i.e.*, 8 *versus* 10.3).[73] Analysis was performed on 50 ns of equilibrated MD. For the $Au_{25}$(Peptide)$_{18}$ nanoclusters, all 18 peptide-ligands are anchored to gold *via* their protonated N-terminal cysteines (Figure 1a), and 200 ns of equilibrated conformations were used for the analysis of each system.

Simulations for methylammonium free-in-solution followed our previously described simulation protocol,[70] except using the all-atom AMBER99SB-ILDN force field to maintain consistency with the MD simulations of the $Au_{25}$(Peptide)$_{18}$ models and CVVGDD in solution. Statistics from 25 ns of equilibrated MD was used for analysis.

## ASSOCIATED CONTENT

### Supporting Information

The Supporting Information is available free of charge on the ACS Publications website.

Additional information of MD parameters and settings; adapted figures of our previous MD results[65] emphasising differences in peptide-conformation, surface-bound water molecules, and distribution of electron-rich/electron-deficient atoms around the Au kernels of the various $Au_{25}$(Peptide)$_{18}$ systems (PDF)

## AUTHOR INFORMATION


### Corresponding Authors

**Irene Yarovsky** – *School of Engineering, RMIT University, Victoria 3001, Australia*; orcid.org/0000-0002-4033-5150;
Email: irene.yarovsky@rmit.edu.au

**Stefano Corni** – *Dipartimento di Scienze Chimiche, Università di Padova, 35131 Padova, Italy*; *Istituto di Nanoscienze, Consiglio Nazionale delle Ricerche CNR-NANO, 41125 Modena, Italy*; orcid.org/0000-0001-6707-108X;
Email: stefano.corni@unipd.it

### Authors

**Laura Zanetti-Polzi** – *Istituto di Nanoscienze, Consiglio Nazionale delle Ricerche CNR-NANO, 41125 Modena, Italy*; orcid.org/0000-0002-2550-4796

**Patrick Charchar** – *School of Engineering, RMIT University, Victoria 3001, Australia*; orcid.org/0000-0002-9201-4711


### Author Contributions

[⊥]L.Z.P. and P.C. contributed equally to this work. The manuscript was written through contributions of all authors. All authors have given approval to the final version of the manuscript.

### Notes

The authors declare no competing financial interest.

**Table 2. Deprotonation processes investigated using the Molecular Dynamics–Perturbed Matrix Method (MD-PMM).**

| system | charge state | aqueous deprotonation process: protonated ensemble → deprotonated ensemble |
|---|---|---|
| *amine* | | |
| methylammonium[a] | +1 → 0 | $CH_3\mathbf{NH_3^+}$ → $CH_3\mathbf{NH_2}$ |
| CVVGDD[b] | +1:–2 → 0:–2 | $^+\mathbf{H_3N}$–(Pep)$^{-2}$ → $\mathbf{H_2N}$–(Pep)$^{-2}$ |
| $Au_{25}$(CVVGDD)$_{18}$[c] | +1:–36 → 0:–36 | $Au_{25}(H_2N\text{–(Pep)}^{-2})_{17}(^+\mathbf{H_3N}\text{–(Pep)}^{-2})_1$ → $Au_{25}(\mathbf{H_2N}\text{–(Pep)}^{-2})_{18}$ |
| $Au_{25}$(Peptide)$_{18}$[d] | +18:–36 → +17:–36 | $Au_{25}(^+\mathbf{H_3N}\text{–(Pep)}^{-2})_{18}$ → $Au_{25}(^+H_3N\text{–(Pep)}^{-2})_{17}(\mathbf{H_2N}\text{–(Pep)}^{-2})_1$ |
| *carboxyl* | | |
| $Au_{25}$(Peptide)$_{18}$[e] | +18:–35 → +18:–36 | $Au_{25}(^+H_3N\text{–(Pep)}^{-2})_{17}(^+H_3N\text{–(Pep)}^{-1})_1$ → $Au_{25}(^+H_3N\text{–(Pep)}^{-2})_{18}$ |

[a]Reference calculation (free-in-solution). [b]N-terminal amine of CVVGDD peptide (free-in-solution). [c]N-terminal amine of CVVGDD ligand to the "fully deprotonated" microstate (0:–36). [d]N-terminal amine from the "zwitterion" microstate (+18:–36), repeated for the 18 ligands. [e]Asparate carboxyl sidechain to the "zwitterion" microstate, repeated for the two aspartic acids in each of the 18 ligands. [d,e]Peptide = CYYGDD, CVVGDD, or CGGGDD.

## ACKNOWLEDGMENTS

I.Y. acknowledges the Australian Research Council for financial support under the Discovery Project scheme (DP170100511). This research was undertaken with the assistance of resources from the National Computational Infrastructure (NCI) (grant e87). P.C. gratefully acknowledges School of Engineering, RMIT University and Dipartimento di Scienze Chimiche, Università di Padova for travel support.

## REFERENCES

(1) Jin, R. Atomically Precise Metal Nanoclusters: Stable Sizes and Optical Properties. *Nanoscale* **2015**, *7*, 1549–1565.

(2) Yamazoe, S.; Takano, S.; Kurashige, W.; Yokoyama, T.; Nitta, K.; Negishi, Y.; Tsukuda, T. Hierarchy of Bond Stiffnesses within Icosahedral-Based Gold Clusters Protected by Thiolates. *Nat. Commun.* **2016**, *7*, 10414.

(3) Weerawardene, K. L. D. M.; Häkkinen, H.; Aikens, C. M. Connections between Theory and Experiment for Gold and Silver Nanoclusters. *Annu. Rev. Phys. Chem.* **2018**, *69*, 205–229.

(4) Olesiak-Banska, J.; Waszkielewicz, M.; Obstarczyk, P.; Samoc, M. Two-Photon Absorption and Photoluminescence of Colloidal Gold Nanoparticles and Nanoclusters. *Chem. Soc. Rev.* **2019**, *48*, 4087–4117.

(5) Zhou, M.; Du, X.; Wang, H.; Jin, R. The Critical Number of Gold Atoms for a Metallic State Nanocluster: Resolving a Decades-Long Question. *ACS Nano* **2021**, *15*, 13980–13992.

(6) Zheng, K.; Setyawati, M. I.; Leong, D. T.; Xie, J. Antimicrobial Gold Nanoclusters. *ACS Nano* **2017**, *11*, 6904–6910.

(7) Yahia-Ammar, A.; Sierra, D.; Mérola, F.; Hildebrandt, N.; Le Guével, X. Self-Assembled Gold Nanoclusters for Bright Fluorescence Imaging and Enhanced Drug Delivery. *ACS Nano* **2016**, *10*, 2591–2599.

(8) Matus, M. F.; Häkkinen, H. Atomically Precise Gold Nanoclusters: Towards an Optimal Biocompatible System from a Theoretical–Experimental Strategy. *Small* **2021**, e2005499.

(9) Lin, Z.; Goswami, N.; Xue, T.; Chai, O. J. H.; Xu, H.; Liu, Y.; Su, Y.; Xie, J. Engineering Metal Nanoclusters for Targeted Therapeutics: From Targeting Strategies to Therapeutic Applications. *Adv. Funct. Mater.* **2021**, *31*, 2105662.

(10) Du, Y.; Sheng, H.; Astruc, D.; Zhu, M. Atomically Precise Noble Metal Nanoclusters as Efficient Catalysts: A Bridge between Structure and Properties. *Chem. Rev.* **2020**, *120*, 526–622.

(11) Jiang, D.-e. Staple Fitness: A Concept to Understand and Predict the Structures of Thiolated Gold Nanoclusters. *Chem. Eur. J.* **2011**, *17*, 12289–12293.

(12) Natarajan, G.; Mathew, A.; Negishi, Y.; Whetten, R. L.; Pradeep, T. A Unified Framework for Understanding the Structure and Modifications of Atomically Precise Monolayer Protected Gold Clusters. *J. Phys. Chem. C* **2015**, *119*, 27768–27785.

(13) Xu, W. W.; Zhu, B.; Zeng, X. C.; Gao, Y. A Grand Unified Model for Liganded Gold Clusters. *Nat. Commun.* **2016**, *7*, 13574.

(14) Chakraborty, I.; Pradeep, T. Atomically Precise Clusters of Noble Metals: Emerging Link between Atoms and Nanoparticles. *Chem. Rev.* **2017**, *117*, 8208–8271.

(15) Tang, Q.; Hu, G.; Fung, V.; Jiang, D.-e. Insights into Interfaces, Stability, Electronic Properties, and Catalytic Activities of Atomically Precise Metal Nanoclusters from First Principles. *Acc. Chem. Res.* **2018**, *51*, 2793–2802.

(16) Merz, S. N.; Farrell, Z. J.; Pearring, J.; Hoover, E.; Kester, M.; Egorov, S. A.; Green, D. L.; DuBay, K. H. Computational and Experimental Investigation of Janus-Like Monolayers on Ultrasmall Noble Metal Nanoparticles. *ACS Nano* **2018**, *12*, 11031–11040.

(17) Agrachev, M.; Ruzzi, M.; Venzo, A.; Maran, F. Nuclear and Electron Magnetic Resonance Spectroscopies of Atomically Precise Gold Nanoclusters. *Acc. Chem. Res.* **2019**, *52*, 44–52.

(18) Pei, Y.; Wang, P.; Ma, Z.; Xiong, L. Growth-Rule-Guided Structural Exploration of Thiolate-Protected Gold Nanoclusters. *Acc. Chem. Res.* **2019**, *52*, 23–33.

(19) Riccardi, L.; De Biasi, F.; De Vivo, M.; Burgi, T.; Rastrelli, F.; Salassa, G. Dynamic Origin of Chirality Transfer between Chiral Surface and Achiral Ligand in $Au_{38}$ Clusters. *ACS Nano* **2019**, *13*, 7127–7134.

(20) Takano, S.; Tsukuda, T. Chemically Modified Gold/Silver Superatoms as Artificial Elements at Nanoscale: Design Principles and Synthesis Challenges. *J. Am. Chem. Soc.* **2021**, *143*, 1683–1698.

(21) Reimers, J. R.; Ford, M. J.; Halder, A.; Ulstrup, J.; Hush, N. S. Gold Surfaces and Nanoparticles Are Protected by Au(0)–Thiyl Species and Are Destroyed When Au(I)–Thiolates Form. *Proc. Natl. Acad. Sci. U. S. A.* **2016**, *113*, E1424–E1433.

(22) Häkkinen, H. The Gold–Sulfur Interface at the Nanoscale. *Nat. Chem.* **2012**, *4*, 443–455.

(23) Kang, X.; Chong, H.; Zhu, M. $Au_{25}(SR)_{18}$: The Captain of the Great Nanocluster Ship. *Nanoscale* **2018**, *10*, 10758–10834.

(24) Heaven, M. W.; Dass, A.; White, P. S.; Holt, K. M.; Murray, R. W. Crystal Structure of the Gold Nanoparticle $[N(C_8H_{17})_4][Au_{25}(SCH_2CH_2Ph)_{18}]$. *J. Am. Chem. Soc.* **2008**, *130*, 3754–3755.

(25) Zhu, M.; Aikens, C. M.; Hollander, F. J.; Schatz, G. C.; Jin, R. Correlating the Crystal Structure of a Thiol-Protected $Au_{25}$ Cluster and Optical Properties. *J. Am. Chem. Soc.* **2008**, *130*, 5883–5885.

(26) Collins, C. B.; Tofanelli, M. A.; Crook, M. F.; Phillips, B. D.; Ackerson, C. J. Practical Stability of $Au_{25}(SR)_{18}^{-1/0/+1}$. *RSC Adv.* **2017**, *7*, 45061–45065.

(27) Salassa, G.; Sels, A.; Mancin, F.; Burgi, T. Dynamic Nature of Thiolate Monolayer in $Au_{25}(SR)_{18}$ Nanoclusters. *ACS Nano* **2017**, *11*, 12609–12614.

(28) Li, G.; Abroshan, H.; Liu, C.; Zhuo, S.; Li, Z.; Xie, Y.; Kim, H. J.; Rosi, N. L.; Jin, R. Tailoring the Electronic and Catalytic Properties of $Au_{25}$ Nanoclusters *via* Ligand Engineering. *ACS Nano* **2016**, *10*, 7998–8005.

(29) Zhang, B.; Chen, J.; Cao, Y.; Chai, O. J. H.; Xie, J. Ligand Design in Ligand-Protected Gold Nanoclusters. *Small* **2021**, e2004381.

(30) Wu, Z.; Jin, R. On the Ligand's Role in the Fluorescence of Gold Nanoclusters. *Nano Lett.* **2010**, *10*, 2568–2573.

(31) Yi, C.; Zheng, H.; Herbert, P. J.; Chen, Y.; Jin, R.; Knappenberger, K. L., Jr. Ligand- and Solvent-Dependent Electronic Relaxation Dynamics of $Au_{25}(SR)_{18}^{-}$ Monolayer-Protected Clusters. *J. Phys. Chem. C* **2017**, *121*, 24894–24902.

(32) Pramanik, G.; Humpolickova, J.; Valenta, J.; Kundu, P.; Bals, S.; Bour, P.; Dracinsky, M.; Cigler, P. Gold Nanoclusters with Bright Near-Infrared Photoluminescence. *Nanoscale* **2018**, *10*, 3792–3798.

(33) Aikens, C. M. Electronic and Geometric Structure, Optical Properties, and Excited State Behavior in Atomically Precise Thiolate-Stabilized Noble Metal Nanoclusters. *Acc. Chem. Res.* **2018**, *51*, 3065–3073.

(34) Kang, X.; Zhu, M. Tailoring the Photoluminescence of Atomically Precise Nanoclusters. *Chem. Soc. Rev.* **2019**, *48*, 2422–2457.

(35) Muñoz-Castro, A. On the Ligand–Core Interaction in Ligand-Protected Gold Superatoms. Insights from $Au_{25}(XR)_{18}$ (X = S, Se, Te) via Relativistic DFT Calculations. *Phys. Chem. Chem. Phys.* **2019**, *21*, 13022–13029.

(36) Zhu, S.; Wang, X.; Cong, Y.; Li, L. Regulating the Optical Properties of Gold Nanoclusters for Biological Applications. *ACS Omega* **2020**, *5*, 22702–22707.

(37) Porret, E.; Sancey, L.; Martín-Serrano, A.; Montañez, M. I.; Seeman, R.; Yahia-Ammar, A.; Okuno, H.; Gomez, F.; Ariza, A.; Hildebrandt, N.; Fleury, J.-B.; Coll, J.-L.; Le Guével, X. Hydrophobicity of Gold Nanoclusters Influences Their Interactions with Biological Barriers. *Chem. Mater.* **2017**, *29*, 7497–7506.

(38) Cowan, M. J.; Higaki, T.; Jin, R.; Mpourmpakis, G. Understanding the Solubility Behavior of Atomically Precise Gold Nanoclusters. *J. Phys. Chem. C* **2019**, *123*, 20006–20012.

(39) Gao, G.; Liu, X.; Gu, Z.; Mu, Q.; Zhu, G.; Zhang, T.; Zhang, C.; Zhou, L.; Shen, L.; Sun, T. Engineering Nanointerfaces of $Au_{25}$ Clusters for Chaperone-Mediated Peptide Amyloidosis. *Nano Lett.* **2022**, *22*, 2964–2970.

(40) Jin, R.; Li, G.; Sharma, S.; Li, Y.; Du, X. Toward Active-Site Tailoring in Heterogeneous Catalysis by Atomically Precise Metal Nanoclusters with Crystallographic Structures. *Chem. Rev.* **2021**, *121*, 567–648.

(41) Li, Y.; Jin, R. Seeing Ligands on Nanoclusters and in Their Assemblies by X-ray Crystallography: Atomically Precise Nanochemistry and Beyond. *J. Am. Chem. Soc.* **2020**, *142*, 13627–13644.

(42) Hirata, K.; Yamashita, K.; Muramatsu, S.; Takano, S.; Ohshimo, K.; Azuma, T.; Nakanishi, R.; Nagata, T.; Yamazoe, S.; Koyasu, K.; Tsukuda, T. Anion Photoelectron Spectroscopy of Free $[Au_{25}(SC_{12}H_{25})_{18}]^{-}$. *Nanoscale* **2017**, *9*, 13409–13412.

(43) Bhat, S.; Narayanan, R. P.; Baksi, A.; Chakraborty, P.; Paramasivam, G.; Methikkalam, R. R. J.; Nag, A.; Natarajan, G.; Pradeep, T. Detection of $[Au_{25}(PET)_{18}(O_2)_N]^{-}$ ($N$ = 1, 2, 3) Species by Mass Spectrometry. *J. Phys. Chem. C* **2018**, *122*, 19455–19462.

(44) Matsuyama, T.; Hirayama, J.; Fujiki, Y.; Kikkawa, S.; Kurashige, W.; Asakura, H.; Kawamura, N.; Negishi, Y.; Nakatani, N.; Hatada, K.; Ota, F.; Yamazoe, S. Effect of Ligand on the Electronic State of Gold in Ligand-Protected Gold Clusters Elucidated by X-ray Absorption Spectroscopy. *J. Phys. Chem. C* **2021**, *125*, 3143–3149.

(45) Dou, X.; Chen, X.; Zhu, H.; Liu, Y.; Chen, D.; Yuan, X.; Yao, Q.; Xie, J. Water-Soluble Metal Nanoclusters: Recent Advances in Molecular-Level Exploration and Biomedical Applications. *Dalton Trans.* **2019**, *48*, 10385–10392.

(46) Porret, E.; Le Guével, X.; Coll, J.-L. Gold Nanoclusters for Biomedical Applications: Toward in Vivo Studies. *J. Mater. Chem. B* **2020**, *8*, 2216–2232.

(47) Yuan, Q.; Wang, Y.; Zhao, L.; Liu, R.; Gao, F.; Gao, L.; Gao, X. Peptide Protected Gold Clusters: Chemical Synthesis and Biomedical Applications. *Nanoscale* **2016**, *8*, 12095–12104.

(48) Liu, X.; Zhang, Q.; Knoll, W.; Liedberg, B.; Wang, Y. Rational Design of Functional Peptide–Gold Hybrid Nanomaterials for Molecular Interactions. *Adv. Mater.* **2020**, *32*, e2000866.

(49) Loynachan, C. N.; Soleimany, A. P.; Dudani, J. S.; Lin, Y.; Najer, A.; Bekdemir, A.; Chen, Q.; Bhatia, S. N.; Stevens, M. M. Renal Clearable Catalytic Gold Nanoclusters for in Vivo Disease Monitoring. *Nat. Nanotechnol.* **2019**, *14*, 883–890.

(50) Chen, W.; Tu, X.; Guo, X. Fluorescent Gold Nanoparticles-Based Fluorescence Sensor for $Cu^{2+}$ Ions. *Chem. Commun.* **2009**, 1736–1738.

(51) Charchar, P.; Christofferson, A. J.; Todorova, N.; Yarovsky, I. Understanding and Designing the Gold–Bio Interface: Insights from Simulations. *Small* **2016**, *12*, 2395–2418.

(52) Juarez-Mosqueda, R.; Mpourmpakis, G. Elucidating the Optical Spectra of $[Au_{25}(SR)_{18}]^q$ Nanoclusters. *Phys. Chem. Chem. Phys.* **2019**, *21*, 22272–22282.

(53) Matus, M. F.; Malola, S.; Kinder Bonilla, E.; Barngrover, B. M.; Aikens, C. M.; Häkkinen, H. A Topological Isomer of the $Au_{25}(SR)_{18}^-$ Nanocluster. *Chem. Commun.* **2020**, *56*, 8087–8090.

(54) Ahmad, S. N.; Zaharim, W. N.; Sulaiman, S.; Hasan Baseri, D. F.; Mohd Rosli, N. A.; Ang, L. S.; Yahaya, N. Z.; Watanabe, I. Density Functional Theory Studies of the Electronic Structure and Muon Hyperfine Interaction in $[Au_{25}(SR)_{18}]^0$ and $[Au_{25}(SeR)_{18}]^0$ Nanoclusters. *ACS Omega* **2020**, *5*, 33253–33261.

(55) Weerawardene, K. L. D. M.; Aikens, C. M. Theoretical Insights into the Origin of Photoluminescence of $Au_{25}(SR)_{18}^-$ Nanoparticles. *J. Am. Chem. Soc.* **2016**, *138*, 11202–11210.

(56) Ebina, M.; Iwasa, T.; Harabuchi, Y.; Taketsugu, T. Time-Dependent Density Functional Theory Study on Higher Low-Lying Excited States of $Au_{25}(SR)_{18}^-$. *J. Phys. Chem. C* **2018**, *122*, 4097–4104.

(57) Austin, N.; Zhao, S.; McKone, J. R.; Jin, R.; Mpourmpakis, G. Elucidating the Active Sites for $CO_2$ Electroreduction on Ligand-Protected $Au_{25}$ Nanoclusters. *Catal. Sci. Technol.* **2018**, *8*, 3795–3805.

(58) Vanzan, M.; Corni, S. Role of Organic Ligands Orientation on the Geometrical and Optical Properties of $Au_{25}(SCH_3)_{18}^0$. *J. Phys. Chem. A* **2018**, *122*, 6864–6872.

(59) Senanayake, R. D.; Aikens, C. M. Electronic Relaxation Dynamics in $[Au_{25}(SR)_{18}]^{-1}$ (R = $CH_3$, $C_2H_5$, $C_3H_7$, MPA, PET) Thiolate-Protected Nanoclusters. *Phys. Chem. Chem. Phys.* **2020**, *22*, 5272–5285.

(60) Brancolini, G.; Toroz, D.; Corni, S. Can Small Hydrophobic Gold Nanoparticles Inhibit $\beta_2$-Microglobulin Fibrillation? *Nanoscale* **2014**, *6*, 7903–7911.

(61) An, D.; Su, J.; Weber, J. K.; Gao, X.; Zhou, R.; Li, J. A Peptide-Coated Gold Nanocluster Exhibits Unique Behavior in Protein Activity Inhibition. *J. Am. Chem. Soc.* **2015**, *137*, 8412–8418.

(62) Vanzan, M.; Rosa, M.; Corni, S. Atomistic Insight into the Aggregation of $[Au_{25}\ (SR)_{18}]^q$ Nanoclusters. *Nanoscale Adv.* **2020**, *2*, 2842–2852.

(63) Liu, M.; Gao, L.; Zhao, L.; He, J.; Yuan, Q.; Zhang, P.; Zhao, Y.; Gao, X. Peptide-Au Clusters Induced Tumor Cells Apoptosis via Targeting Glutathione Peroxidase-1: The Molecular Dynamics Assisted Experimental Studies. *Sci. Rep.* **2017**, *7*, 131.

(64) Rojas-Cervellera, V.; Rovira, C.; Akola, J. How Do Water Solvent and Glutathione Ligands Affect the Structure and Electronic Properties of $Au_{25}(SR)_{18}^-$? *J. Phys. Chem. Lett.* **2015**, *6*, 3859–3865.

(65) Lin, Y.; Charchar, P.; Christofferson, A. J.; Thomas, M. R.; Todorova, N.; Mazo, M. M.; Chen, Q.; Doutch, J.; Richardson, R.; Yarovsky, I.; Stevens, M. M. Surface Dynamics and Ligand–Core Interactions of Quantum Sized Photoluminescent Gold Nanoclusters. *J. Am. Chem. Soc.* **2018**, *140*, 18217–18226.

(66) Zanetti-Polzi, L.; Del Galdo, S.; Daidone, I.; D'Abramo, M.; Barone, V.; Aschi, M.; Amadei, A. Extending the Perturbed Matrix Method Beyond the Dipolar Approximation: Comparison of Different Levels of Theory. *Phys. Chem. Chem. Phys.* **2018**, *20*, 24369–24378.

(67) Zanetti-Polzi, L.; Bortolotti, C. A.; Daidone, I.; Aschi, M.; Amadei, A.; Corni, S. A Few Key Residues Determine the High Redox Potential Shift in Azurin Mutants. *Org. Biomol. Chem.* **2015**, *13*, 11003–11013.

(68) Paltrinieri, L.; Di Rocco, G.; Battistuzzi, G.; Borsari, M.; Sola, M.; Ranieri, A.; Zanetti-Polzi, L.; Daidone, I.; Bortolotti, C. A. Computational Evidence Support the Hypothesis of Neuroglobin Also Acting as an Electron Transfer Species. *J. Biol. Inorg. Chem.* **2017**, *22*, 615–623.

(69) Zanetti-Polzi, L.; Daidone, I.; Bortolotti, C. A.; Corni, S. Surface Packing Determines the Redox Potential Shift of Cytochrome C Adsorbed on Gold. *J. Am. Chem. Soc.* **2014**, *136*, 12929–12937.

(70) Zanetti-Polzi, L.; Daidone, I.; Amadei, A. Fully Atomistic Multiscale Approach for p$K_a$ Prediction. *J. Phys. Chem. B* **2020**, *124*, 4712–4722.

(71) *Lange's Handbook of Chemistry*. 11th ed.; McGraw-Hill Inc.: New York, 1973.

(72) Lindorff-Larsen, K.; Piana, S.; Palmo, K.; Maragakis, P.; Klepeis, J. L.; Dror, R. O.; Shaw, D. E. Improved Side-Chain Torsion Potentials for the Amber ff99SB Protein Force Field. *Proteins: Struct. Funct. Bioinf.* **2010**, *78*, 1950–1958.

(73) Lide, D. R., *CRC Handbook of Chemistry and Physics*. 72nd ed.; CRC Press: Boca Raton, FL, USA, 1991.

(74) Borkovec, M.; Jonsson, B.; Koper, G. J. M., Ionization Processes and Proton Binding in Polyprotic Systems: Small Molecules, Proteins, Interfaces, and Polyelectrolytes. In *Surface and Colloid Science*, 1st ed.; Springer New York, NY: **2001**; Vol. 16, 99–339.

(75) Pahari, S.; Sun, L.; Alexov, E. PKAD: A Database of Experimentally Measured pKa Values of Ionizable Groups in Proteins. *Database* **2019**, *2019*, baz024.

(76) Pinitglang, S.; Watts, A. B.; Patel, M.; Reid, J. D.; Noble, M. A.; Gul, S.; Bokth, A.; Naeem, A.; Patel, H.; Thomas, E. W.; Sreedharan, S. K.; Verma, C.; Brocklehurst, K. A Classical Enzyme Active Center Motif Lacks Catalytic Competence until Modulated Electrostatically. *Biochemistry* **1997**, *36*, 9968–9982.

(77) Grimsley, G. R.; Scholtz, J. M.; Pace, C. N. A Summary of the Measured p*K* Values of the Ionizable Groups in Folded Proteins. *Protein Sci.* **2009**, *18*, 247–251.

(78) Di Nardo, G.; Breitner, M.; Bandino, A.; Ghosh, D.; Jennings, G. K.; Hackett, J. C.; Gilardi, G. Evidence for an Elevated Aspartate p$K_a$ in the Active Site of Human Aromatase. *J. Biol. Chem.* **2015**, *290*, 1186–1196.

(79) Grytsyk, N.; Sugihara, J.; Kaback, H. R.; Hellwig, P. $pK_a$ of Glu325 in LacY. *Proc. Natl. Acad. Sci. U. S. A.* **2017**, *114*, 1530–1535.

(80) Qin, J.; Clore, G. M.; Gronenborn, A. M. Ionization Equilibria for Side-Chain Carboxyl Groups in Oxidized and Reduced Human Thioredoxin and in the Complex with Its Target Peptide from the Transcription Factor NFκB. *Biochemistry* **1996**, *35*, 7–13.

(81) García-Moreno, B. E.; Dwyer, J. J.; Gittis, A. G.; Lattman, E. E.; Spencer, D. S.; Stites, W. E. Experimental Measurement of the Effective Dielectric in the Hydrophobic Core of a Protein. *Biophys. Chem.* **1997**, *64*, 211–224.

(82) Dao-pin, S.; Anderson, D. E.; Baase, W. A.; Dahlquist, F. W.; Matthews, B. W. Structural and Thermodynamic Consequences of Burying a Charged Residue within the Hydrophobic Core of T4 Lysozyme. *Biochemistry* **1991**, *30*, 11521–11529.

(83) Zanetti-Polzi, L.; Corni, S.; Daidone, I.; Amadei, A. Extending the Essential Dynamics Analysis to Investigate Molecular Properties: Application to the Redox Potential of Proteins. *Phys. Chem. Chem. Phys.* **2016**, *18*, 18450–18459.

(84) Koper, G. J. M.; Borkovec, M. Proton Binding by Linear, Branched, and Hyperbranched Polyelectrolytes. *Polymer* **2010**, *51*, 5649–5662.

(85) Amadei, A.; D'Abramo, M.; Daidone, I.; D'Alessandro, M.; Nola, A. D.; Aschi, M. Statistical Mechanical Modelling of Chemical Reactions in Complex Systems: The Kinetics of the Haem Carbon Monoxide Binding–Unbinding Reaction in Myoglobin. *Theor. Chem. Acc.* **2007**, *117*, 637–647.

(86) Amadei, A.; Daidone, I.; Aschi, M. A General Theoretical Model for Electron Transfer Reactions in Complex Systems. *Phys. Chem. Chem. Phys.* **2012**, *14*, 1360–1370.

(87) Aschi, M.; D'Abramo, M.; Ramondo, F.; Daidone, I.; D'Alessandro, M.; Di Nola, A.; Amadei, A. Theoretical Modeling of Chemical Reactions in Complex Environments: The Intramolecular Proton Transfer in Aqueous Malonaldehyde. *J. Phys. Org. Chem.* **2006**, *19*, 518–530.

(88) Frisch, M. J.; et al. *Gaussian 09, Revision C.01*, Gaussian, Inc.: Wallingford, CT, USA, 2010.

(89) Parr, R. G.; Yang, W. Density-Functional Theory of the Electronic Structure of Molecules. *Annu. Rev. Phys. Chem.* **1995**, *46*, 701–728.

(90) Krishnan, R.; Binkley, J. S.; Seeger, R.; Pople, J. A. Self - Consistent Molecular Orbital Methods. XX. A Basis Set for Correlated Wave Functions. *J. Chem. Phys.* **1980**, *72*, 650-654.

(91) Becke, A. D. Density-Functional Thermochemistry. III. The Role of Exact Exchange. *J. Chem. Phys.* **1993**, *98*, 5648–5652.

(92) Besler, B. H.; Merz, K. M.; Kollman, P. A. Atomic Charges Derived from Semiempirical Methods. *J. Comput. Chem.* **1990**, *11*, 431–439.

(93) Hess, B.; Kutzner, C.; van der Spoel, D.; Lindahl, E. GROMACS 4: Algorithms for Highly Efficient, Load-Balanced, and Scalable Molecular Simulation. *J. Chem. Theory Comput.* **2008**, *4*, 435–447.

## TABLE OF CONTENTS